Ultrafine eutectic Ti-Fe-based alloys processed by additive manufacturing – A new candidate for high temperature applications

Joachim Gussone [a,*], Katrin Bugelnig [a], Pere Barriobero-Vila [a], Julio Cesar da Silva [b,f], Ulrike Hecht [c], Christian Dresbach [d], Federico Sket [e], Peter Cloetens [f], Andreas Stark [g], Norbert Schell [g], Jan Haubrich [a], Guillermo Requena [a,h]

[a] German Aerospace Center DLR, Institute of Materials Research, Linder Höhe, 51147 Cologne, Germany
[b] Institut Néel CNRS UPR2940, 25 Avenue des Martyrs BP 166, 38042 Grenoble, France
[c] Access e.V., Intzestr. 5, 52072 Aachen, Germany
[d] University of Applied Sciences Bonn-Rhein-Sieg, Von-Liebig Str. 20, 53359 Rheinbach, Germany
[e] IMDEA Materiales, Eric Kandel 2, Tecnogetafe, 28906 Getafe, Madrid, Spain
[f] European Synchrotron Radiation Facility, 71, Avenue des Martyrs, 38043 Grenoble, France
[g] Helmholtz-Zentrum Geesthacht, Max-Planck-Straße 1, 21502 Geesthacht, Germany
[h] RWTH Aachen University, Metallic Structures and Materials Systems for Aerospace Engineering, D-52062 Aachen, Germany

ARTICLE INFO

ABSTRACT

The development of metals tailored to the metallurgical conditions of laser-based additive manufacturing is crucial to advance the maturity of these materials for their use in structural applications. While efforts in this regard are being carried out around the globe, the use of high strength eutectic alloys have, so far, received minor attention, although previous works showed that rapid solidification techniques can result in ultrafine microstructures with excellent mechanical performance, albeit for small sample sizes. In the present work, a eutectic Ti-32.5Fe alloy has been produced by laser powder bed fusion aiming at exploiting rapid solidification and the capability to produce bulk ultrafine microstructures provided by this processing technique.

Process energy densities between 160 J/mm³ and 180 J/mm³ resulted in a dense and crack-free material with an oxygen content of ~ 0.45 wt.% in which a hierarchical microstructure is formed by μm-sized η-Ti$_4$Fe$_2$O$_x$ dendrites embedded in an ultrafine eutectic β-Ti/TiFe matrix. The microstructure was studied three-dimensionally using near-field synchrotron ptychographic X-ray computed tomography with an actual spatial resolution down to 39 nm to analyse the morphology of the eutectic and dendritic structures as well as to quantify their mass density, size and distribution. Inter-lamellar spacings down to ~ 30–50 nm were achieved, revealing the potential of laser-based additive manufacturing to generate microstructures smaller than those obtained by classical rapid solidification techniques for bulk materials. The alloy was deformed at 600 °C under compressive loading up to a strain of ~ 30% without damage formation, resulting in a compressive yield stress of ~ 800 MPa.

This study provides a first demonstration of the feasibility to produce eutectic Ti-Fe alloys with ultrafine microstructures by laser powder bed fusion that are suitable for structural applications at elevated temperature.

1. Introduction

Studies on ultrafine eutectic titanium-iron-based alloys indicate that very high strengths (>2.5 GPa at room temperature) together with enhanced compressive ductility (>10%) can be achieved [1,2]. So far, binary Ti-Fe [3,4] as well as ternary and quaternary eutec-

* Corresponding author.
E-mail address: Joachim.gussone@dlr.de (J. Gussone).

tic systems have been investigated mainly based on individual or combined additions of Sn and Nb [1,5,6].

In addition, slightly off-eutectic compositions, i.e. hypoeutectic [7] or hypereutectic [8], have been considered for alloy design, resulting in hierarchically structured materials, as their microstructures display features of distinct length scales [9], e.g. primary dendrites embedded in a fine lamellar eutectic matrix. The architecture of these features depends on the growth conditions during solidification. Their grain sizes commonly decrease with increasing growth velocity or cooling rate. This allows significant size-hardening effects and opens a gateway to materials design by rapid solidification techniques.

Although this class of titanium-based eutectic alloys has been investigated for decades, no economically and technically viable processing route for manufacturing large samples or actual components exist and, therefore, none of the proposed alloys is currently mature for industrial applications. Laser-based additive manufacturing, in particular laser powder bed fusion (LPBF), inherently provides very fast solidification and cooling rates, i.e. it may be a suitable method to overcome these issues.

In the present study we demonstrate the processing of Ti-32.5Fe (wt.%) by LPBF and the possibility to produce ultrafine microstructures with attractive mechanical performance. The state-of-the-art characterization methods applied in this work reveal a multi-scale microstructure consisting of μm-sized dendrites embedded in ultrafine eutectic regions. The dendrites consist of the oxygen-stabilized Ti_2Fe phase (η-$Ti_4Fe_2O_x$) that is formed in situ during LPBF. While this phase was observed and characterized in several studies [10–14], its properties profile at elevated temperature is provided here for the first time. Particular emphasis is given to the analysis of the 3D architecture of the microstructural constituents as well as their influence on high temperature deformation behaviour.

2. Material and methods

The experimental methods are introduced concisely in this section. Further details are given in the supplementary materials A1 to A6.

2.1. Powder blending and additive manufacturing

Elemental powders of commercially pure titanium (CP1-Ti, O < 0.18 wt.%, Fe < 0.2 wt.%, N < 0.03 wt.%) and iron (>99.8 wt.%, Ni ~ 0.08 wt.%, Cu ~ 0.06 wt.%) were blended in a glovebox under argon atmosphere to obtain a titanium-rich eutectic composition (Ti-32.5Fe, wt.%).

LPBF was carried out in a SLM Solutions 280 HL machine equipped with a 400 W fibre laser and a heating platform that can reach up to ~ 800 °C. Samples were produced under argon atmosphere (>99.999%) at pre-heat temperatures (T_{PH}) of 200 °C and 790 °C, with sample sizes ($h \times w \times l$) of $4 \times 10 \times 10$ mm^3 and $3 \times 5 \times 5$ mm^3, respectively. The building time per layer was constantly 120 s. The pre-heat temperature is applied at the bottom of a Ti-6Al-4V baseplate. The temperature at the top of the baseplate was measured by a thermocouple before the processing and corresponded to ~ 600 °C in the case of $T_{PH} = 790$ °C. The laser power (P) and the scanning rate (v) were varied using two hatch distances, namely $h = 0.1$ mm and $h = 0.05$ mm. The smallest hatch $h = 0.05$ mm was chosen to enhance mixing of the powder blend without excessive overheating. A wide energy density range between $E_V = 33.3$–311.1 J/mm^3 was covered for sample production ($E_V = P/(h \cdot v \cdot t)$ [15]). The layer thickness (t) was kept constant at 30 μm for all experiments.

2.2. Electron microscopy

Scanning electron microscopy (SEM) was performed in backscattered electron mode (BSE) using a FEI Helios Nanolab 600i dual beam (electron and Ga$^+$) microscope. Electron backscattered electron diffraction (EBSD) was carried out using an accelerating voltage of 20 kV, a sample tilt of 70° and a step size of 40 nm with a Zeiss Ultra 55 SEM system equipped with an Oxford Nordlys II EBSD detector and the Software Aztec v3.3.

Samples for SEM and EBSD were prepared by grinding and polishing using 3 μm diamond and SiO_2 suspensions.

β-Ti and TiFe are not discriminated by EBSD in this study because these phases have very similar lattice parameters that hinder their separation. Processing of the EBSD data was performed using the Oxford software package CHANNEL 5.

2.3. Nanoindentation

Nanoindentation was carried out with a nanomechanical tester ZHN from Asmec / ZwickRoell using a Berkovich indenter. The sample was heat-treated at 1000 °C for 10 min to induce a coarsening of the microstructure (by spheroidisation of the eutectic phases [16]) and thus obtain sufficiently large grains to ensure that the influence of neighbouring grains can be neglected. A force of 3 mN was used for all indents. A mapping of 10 × 10 indents provided an adequate number of results (at least 7 indents / phase) for all phases. The results from indents far from a phase boundary were selected by SEM investigation of the sample after the indentation mapping.

2.4. Near-field ptychographic X-ray computed tomography

Cylinders of 16–18 μm diameter and ~ 40 μm length were extracted from polished surfaces for near-field ptychographic X-ray tomography (NF-PXCT) by focused ion beam (FIB) milling. A FEI Helios Nanolab 600i dual beam (electron and Ga$^+$) microscope was used. A platinum layer was deposited on the surface of the samples before FIB milling. Each sample was attached by Pt deposition to a modified Omniprobe tungsten needle that was mounted onto a Huber sample holder.

The NF-PXCT experiments were performed at the ID16A nano-imaging beamline of the European Synchrotron Radiation Facility (ESRF), France [17] (supplementary material A1). The processing of the tomographic volume of each sample was carried out in three steps: 1) phase retrieval of the near-field ptychographic imaging scan at each tomographic angle [18]; 2) pre-processing of the retrieved tomographic projections including removal of linear phase ramp, phase unwrapping and subpixel image registration of the misplacement of the sample at each angle [19]; 3) tomographic reconstruction (supplementary material A2).

The reconstructed volumes were subsequently pre-processed using bandpass filters available in Fiji [20] and Avizo Fire 9.5 to enhance their quality. After filtering, the volumes were converted from 16 bit to 8 bit. Segmentation of microstructural constituents was carried out using the workflow detailed in the supplementary material A3. The mass density was calculated for each voxel of the reconstructed 16 bit tomograms following the procedure presented in [21] (supplementary material A4).

2.5. High energy synchrotron X-ray diffraction

High energy synchrotron X-ray diffraction (HEXRD) was performed at the beamline P07-HEMS of the synchrotron source PETRA III (Deutsches Elektronen-Synchrotron, DESY, Hamburg, Germany). The diffraction images were acquired using a Perkin Elmer XRD1621 (2048 × 2048 pixels) detector. The experiments were
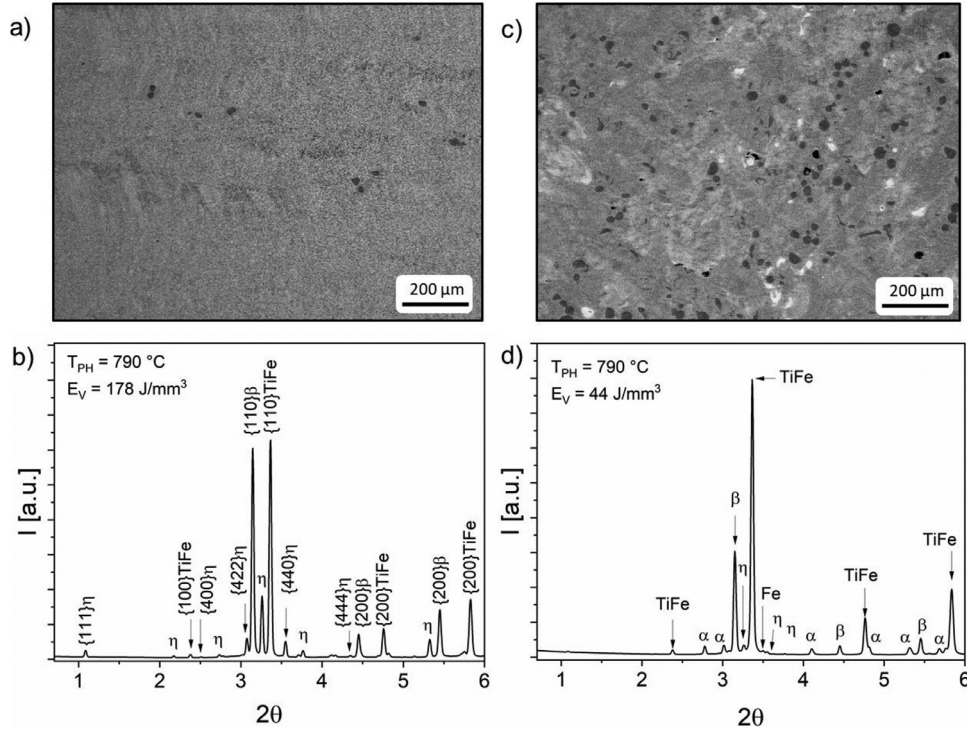
Fig. 1. SEM images (a and c) and HEXRD diffractograms (b and d) of LPBF-Ti-32.5Fe samples produced at T_{PH} = 790 °C with E_V = 178 J/mm^3 (a and b) and E_V = 44 J/mm^3 (c and d). Note that only the reflections used for the evaluation of ε_L shown in Fig. 7 are indexed.

performed in transmission mode using a beam energy of ~ 100 keV (λ = 0.124 Å). The instrumental calibration was obtained using a LaB$_6$ powder standard, azimuthal integration of the diffraction images was carried out with Fit2D and for Rietveld analyses TOPAS 5 was chosen (supplementary material A5).

A modified dilatometer Bähr DIL 805 A/D equipped with an inductive furnace and a deformation unit was used for in-situ HEXRD during compression testing at 600 °C. The experiments were carried out under vacuum ($<10^{-4}$ mbar).

Compression was carried out at a deformation rate of 0.01 s^{-1} and a HEXRD acquisition rate of 2.5 s/image. Cemented carbide discs were used as spacers between the sample (1.5 × 2.5 × 2.5 mm^3) and the silicon nitride stamps. With a beam size of 0.5 × 0.5 mm^2 it was possible to cover a large volume fraction of the sample and avoid measuring local effects. The sample was heated up to 600 °C in 1 min and held at this temperature for 10 min before the deformation started.

The axial lattice strain (ε_L), i.e. parallel to the loading direction, was calculated for each phase based on 2θ variations determined according to Eq. (3) by single peak fitting of individual {hkl} reflections (taking cake portions of ±5° for azimuthal angles ψ = 0° and 180 °C) using a Pseudo-Voigt function:

$$\varepsilon_{\{hkl\},i} = \frac{d_{\{hkl\},\ i} - d_{\{hkl\},0}}{d_{\{hkl\},0}} \qquad (3)$$

where $\varepsilon_{\{hkl\},i}$ and $d_{\{hkl\},i}$ refer to the strain and the interplanar distance of the lattice at the deformation step i, respectively. The d-spacing obtained for the initial condition of the alloy before deformation was used as $d_{\{hkl\},0}$.

Qualitative analysis of the intensity evolution of the diffraction patterns during compression was carried out by converting the Debye–Scherrer rings into Cartesian coordinates (azimuthal angle ψ, 2θ) and subsequently projecting the summed intensities of Bragg reflections on the ψ axis using the software Fiji [20].

Table 1.
Phase fractions (m_f) and Fe contents (C_{Fe}) obtained by HEXRD in the LPBF-Ti-32.5Fe samples.

T_{PH} [°C]	E_V [J/mm^3]	Phase	m_f [wt.%]	C_{Fe} [at.%]
790	44	β-Ti	16.5	11.0
		TiFe	64.8	48.3
		α-Ti	15.3	
		η-Ti$_4$Fe$_2$O$_{0.4}$	2.7	
		Fe	0.6	
790	178	β-Ti	39.5	10.9
		TiFe	40.1	47.7
		α-Ti	1.9	
		η-Ti$_4$Fe$_2$O$_{0.4}$	18.5	
		Fe	0.1	

3. Results

3.1. As-built microstructures

3.1.1. SEM and HEXRD

The variation of pre-heat temperature and energy density resulted in various material conditions. We will focus the analysis on the high temperature processing condition (Fig. 1) because samples without microcracks were successfully obtained only at T_{PH} = 790 °C. Furthermore, low porosity fractions (~ 0.02%) and sufficient mixing of Ti and Fe could only be achieved at high E_V (see representative example in Fig. 1a with E_V = 178 J/mm^3), whereas lower E_V resulted in a very high amount of not fully molten Ti particles (spherical, dark grey) as well as Fe-rich areas that appear bright in the SEM images (Fig. 1c, E_V = 44 J/mm^3).

The insufficient mixing of Ti and Fe (Fig. 1c) at 44 J/mm^3 is also reflected by the considerable fraction of α-Ti determined by HEXRD (Fig. 1d and Table 1) corresponding partially to the α-Ti particles visible in the SEM micrographs. Although there are Fe-rich areas (Fig. 1c, bright areas), the amount of pure Fe is very
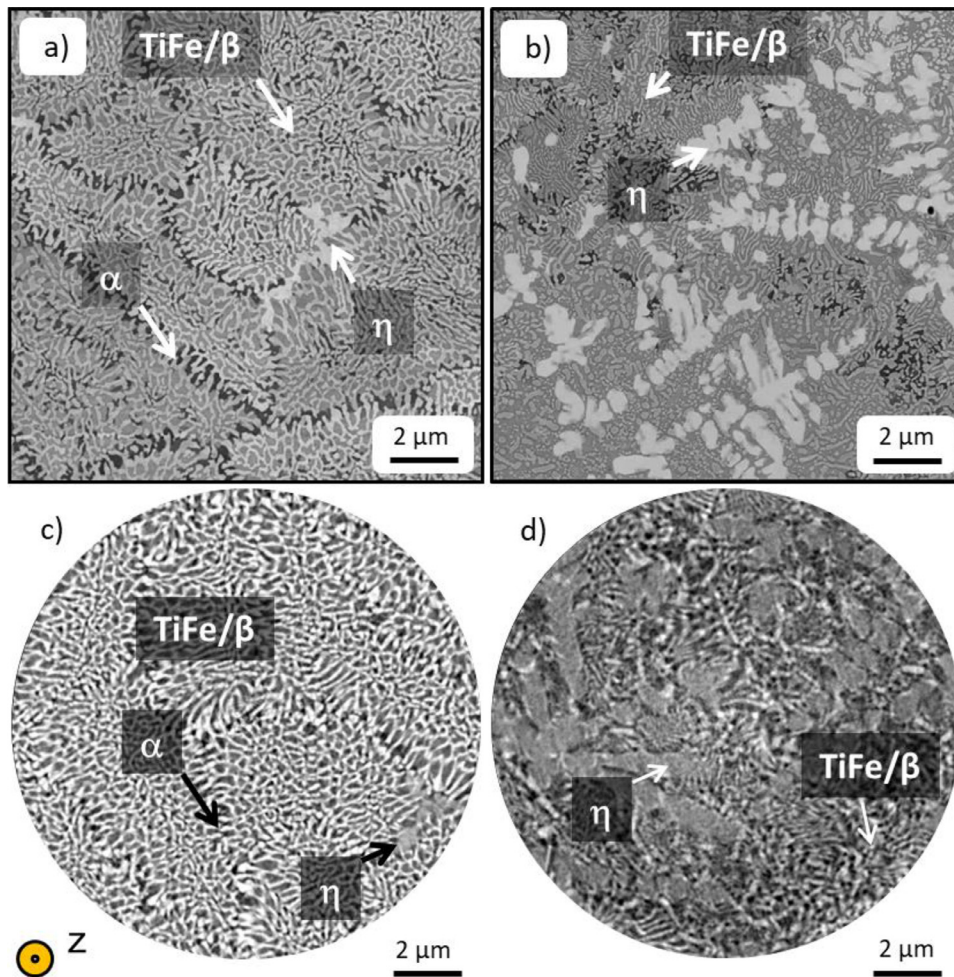
Fig. 2. SEM images (a and b) and xy-slices (building direction (z) perpendicular to the plane of the figure is indicated by the orange arrow) of NF-PXCT reconstructions (c and d) of LPBF-Ti-32.5Fe produced at T_{PH} = 790 °C with high E_V (see Fig. 1a and b). (For interpretation of the references to color in this figure legend, the reader is referred to the web version of this article.)

low (<1 wt.%) according to HEXRD. The β-Ti content is < 20 wt.%, while very high TiFe contents (>60 wt.%) were found for low E_V. Also, small amounts of η-Ti$_4$Fe$_2$O$_x$ were detected by HEXRD (2–3 wt.%) for this manufacturing condition. The formation of this phase was reported in a study dealing with laser-induced synthesis of Ti-Fe powder blends [12] as well as in a eutectic Ti-Fe alloy produced by arc melting [22].

At high energy densities (E_V > 160 J/mm^3), the fraction of β-Ti is similar as that of TiFe (~ 40 wt.%) while the phase fraction of α-Ti is strongly reduced (1–2 wt.%). Moreover, the amount of η-Ti$_4$Fe$_2$O$_x$ at high E_V increased up to almost 20 wt.%. However, similar global oxygen contents were measured for high and low Ev (0.45 wt.% and 0.44 wt.%, respectively) by carrier gas hot extraction (Revierlabor, Essen, Germany) for T_{PH} = 790 °C, i.e. an increase of ~ 0.2 wt.% with respect to the T_{PH} = 200 °C condition. The Fe content (C_{Fe}) in the β-Ti and TiFe phases determined from the lattice parameters is similar for both conditions (Table 1, β-Ti ~ 11 at.% and TiFe ~ 48 at.%).

3.1.2. Near-field ptychographic X-ray computed tomography

The further investigations are focused on microstructures of samples produced at high E_V (160 J/mm^3–180 J/mm^3). The material contains microstructural features of different length scales: SEM micrographs show regions with fine structures in the sub-micrometre range, which are mainly formed by β-Ti and TiFe (Fig. 2a) as well as regions containing η-Ti$_4$Fe$_2$O$_x$ dendrites that extend over several micrometres (Fig. 2b).

The 3D analysis of the microstructure was carried out for the two representative regions shown in Fig. 2a and b. All the phases observable by SEM are also revealed in the NF-PXCT reconstructions (Fig. 2c and d).

The dendritic η-Ti$_4$Fe$_2$O$_x$ phase appears bright in the SEM micrographs (Fig. 2b), whereas the fine TiFe structure corresponds to the brightest features in the NF-PXCT images. The region shown in Fig. 2a and c will be called eutectic-rich (ER) hereafter, while that in Fig. 2b and d will be called dendritic-rich (DR).

Sections through the as-reconstructed NF-PXCT volumes of the ER and DR regions are shown in Fig. 3a and c, while their respective segmentations are presented in Fig. 3b and d. The phases TiFe (blue), β-Ti (green) and small individual α-Ti particles (orange) were clearly segmented in the ER region (Fig. 3b). On the other hand, the fine eutectic phases present in the interdendritic regions of the DR volume reach sizes that are at the limit and even below the spatial resolution (i.e. ~ 48 nm) and were, therefore, omitted in the segmentation procedure. Thus, only the η-Ti$_4$Fe$_2$O$_x$ dendrites are shown in Fig. 3d. Videos of the as-reconstructed and segmented volumes of the ER and DR regions giving a clear overview of the microstructures are provided in the supplementary videos V1 to V4.

A quantitative evaluation reveals that TiFe and β-Ti form highly interconnected 3D networks reaching ~ 99% interconnectiv-
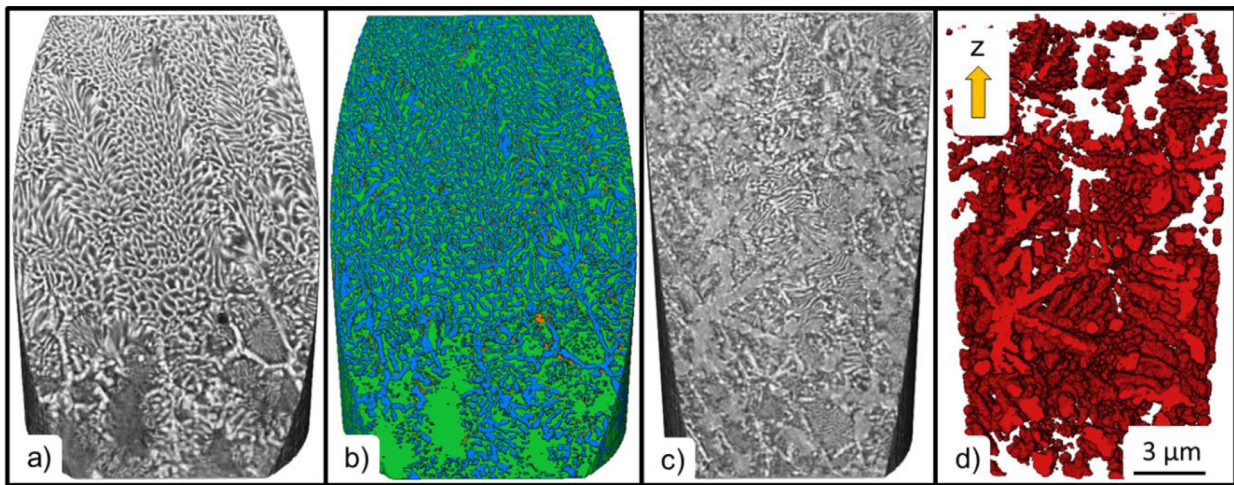
Fig. 3. 3D visualizations of NF-PXCT reconstructions (a and c) and segmentations (b and d) of the phases TiFe (blue), β-Ti (green) and α-Ti (orange) as well as η-Ti$_4$Fe$_2$O$_x$ dendrites (red). Eutectic region, ER (a and b) and dendritic region, DR (c and d). Building direction (z) is indicated by orange arrow (d). (For interpretation of the references to color in this figure legend, the reader is referred to the web version of this article.)
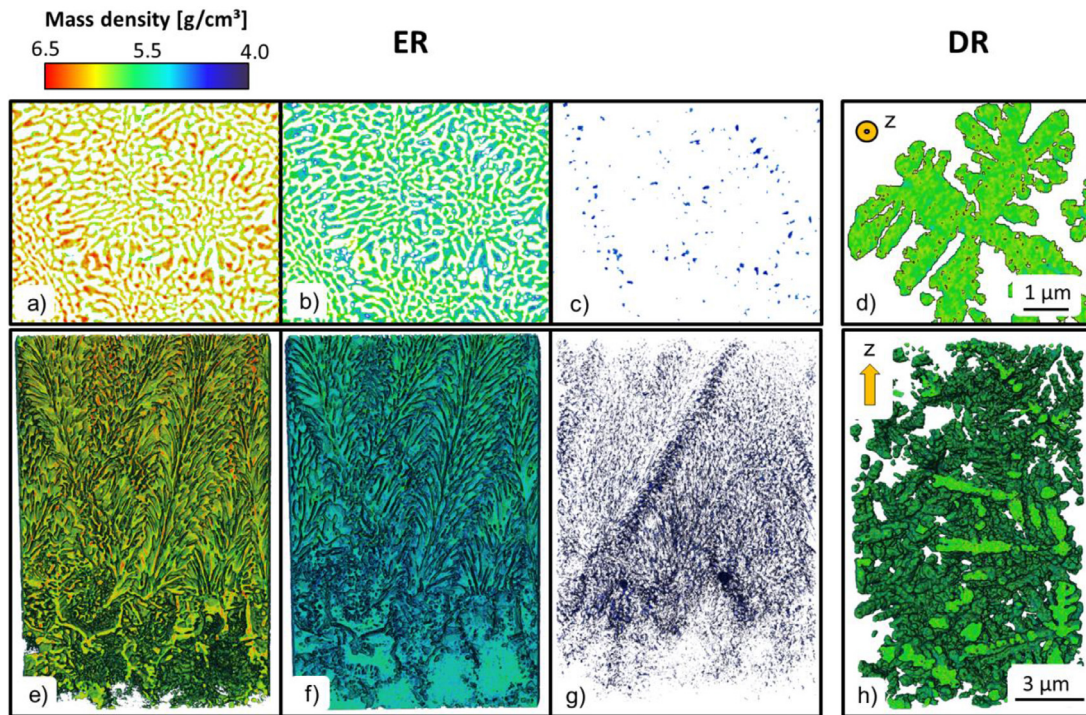

Fig. 4. Mass density maps of xy-slices of NF-PXCT volumes (a - d). 3D visualizations of the mass density (e - f). TiFe (a and e), β-Ti (b and f), α-Ti (c and g) and η-Ti$_4$Fe$_2$O$_x$ (d and h). Eutectic-rich region, ER (a - c) and dendritic-rich region, DR (d). Building direction (z) is indicated by orange arrow (d and h). (For interpretation of the references to color in this figure legend, the reader is referred to the web version of this article.)

ity (largest particle of one phase divided by the total volume fraction of the same phase within the considered volume [23]) in the volumes imaged by NF-PXCT.

The local mass density was calculated from the NF-PXCT images based on the grey values of the reconstructed volumes (supplementary material A4). The segmented phases shown in Fig. 3b and d were converted to colour-coded mass density maps for each phase (Fig. 4).

A sufficiently large region within a phase (far enough from the interface to a second phase) was selected to calculate the local mass density (supplementary material A6). The local mass density determined by this approach is in good agreement with the HEXRD data (Table 2).

Table 2.
Mass densities calculated from NF-PXCT and HEXRD data. Density of LPBF-Ti-32.5Fe calculated with values from Table 1.

Phase	Local ρ (NF-PXCT) [g/cm^3]	Global ρ (HEXRD) [g/cm^3]
α-Ti	4.6 ± 0.08	4.5
β-Ti	5.1 ± 0.09	5.0
η-Ti$_4$Fe$_2$O$_x$	5.5 ± 0.12	5.7
TiFe	6.4 ± 0.13	6.5
LPBF-Ti-32.5Fe	5.62 ± 0.09	5.63

The density ~ 5.62 g/cm^3 of LPBF-Ti-32.5Fe was calculated based on the phase fractions from Table 1. It agrees well with 5.58 ± 0.03 g/cm^3 determined by Archimedes' method.
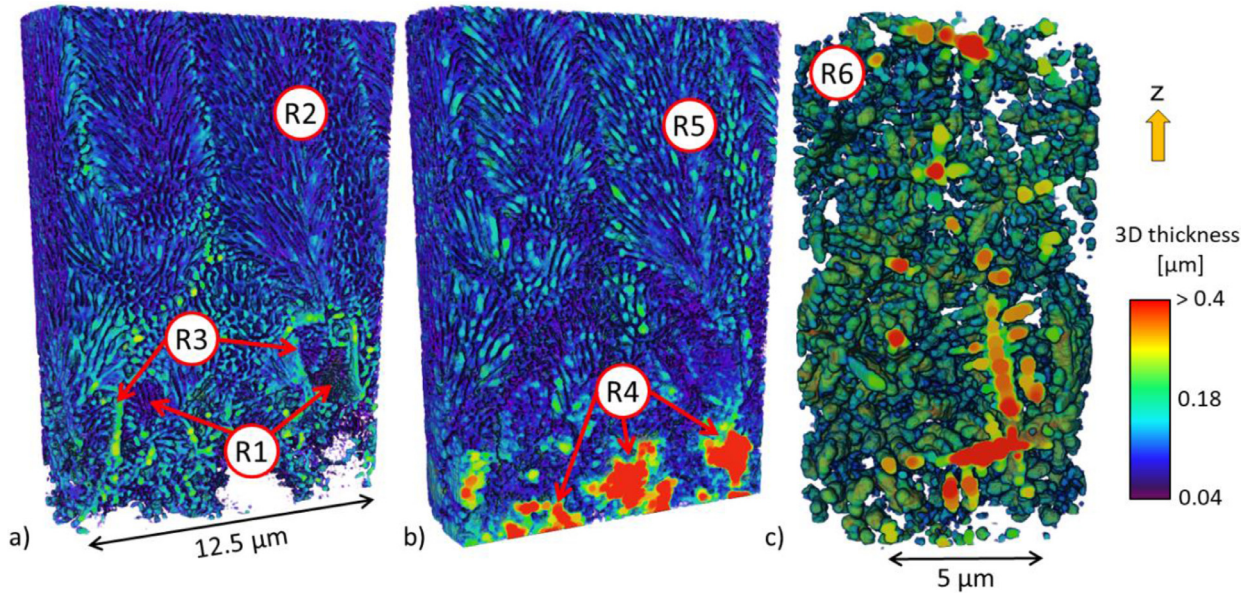
Fig. 5. Colour-coded visualization of 3D thickness in (a) the TiFe network (ER volume), (b) the β–Ti (ER volume) and (c) the η-Ti$_4$Fe$_2$O$_x$ dendrites in the DR volume. Building direction (z) is indicated by orange arrow. (For interpretation of the references to color in this figure legend, the reader is referred to the web version of this article.)
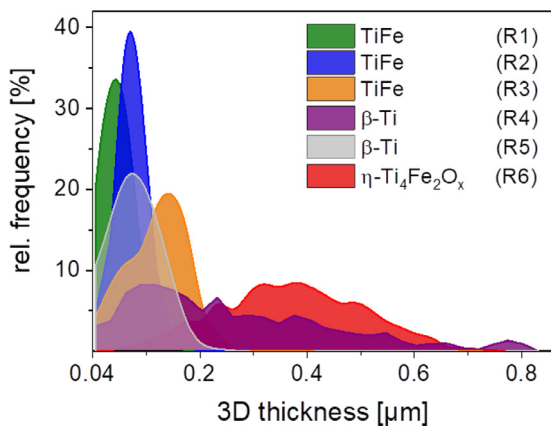

Fig. 6. 3D thickness histograms of the eutectic TiFe-network (R1 – R3), the β-Ti network (R4-R5) and η-Ti$_4$Fe$_2$O$_x$ dendrites (R6) within representative regions marked in Fig. 5. The evaluation is restricted by the resolution limit for the eutectic region (ER), i.e. ~ 40 nm.

A colour-coded visualization of the 3D thickness of the TiFe network (Fig. 5a), the β-Ti network (Fig. 5b) and the η-Ti$_4$Fe$_2$O$_x$ dendrites (Fig. 5c) shows characteristic regions associated with different degrees of microstructural refinement (indicated as R1-R6). The evaluation is restricted to ~ 40 nm, to account for the estimated spatial resolution limit (supplementary material A2). The 3D thickness histograms of these regions are shown in Fig. 6. The eutectic TiFe network in the ER volume shows the finest structures among all segmented phases that are distributed in three regions with clear differences in thickness (Fig. 5a, R1 – R3) and mean 3D thickness of 0.09 $\pm$ 0.03 μm, 0.11 $\pm$ 0.03 μm and 0.16 $\pm$ 0.05 μm for R1 to R3, respectively. It must be reminded that the DR volume even has finer eutectic regions with sizes at the limit of the spatial resolution, which thus were not segmented. The β-Ti phase presents two distinct areas: i) R5, which corresponds to the eutectic β-Ti phase that complements R2 of TiFe, although with a wider thickness distribution (mean 3D thickness = 0.12 $\pm$ 0.05 μm). ii) The coarser globular structures R4. The η-Ti$_4$Fe$_2$O$_x$ dendrites in the DR volume constitute the coarsest structures among all identified

Table 3.
Results of nanoindentation of annealed LPBF-Ti-32.5Fe (T_{PH} = 790 °C, E_V = 178 J/mm^3).

Phase	H [GPa]	E_I (ν = 0.3) [GPa]	H/E_I [1]
β-Ti	6.2 $\pm$ 0.3	152 $\pm$ 5	0.041
TiFe	7.6 $\pm$ 0.7	197 $\pm$ 7	0.038
η-Ti$_4$Fe$_2$O$_x$	12.5 $\pm$ 0.5	202 $\pm$ 7	0.061

phases (R6, corresponding to the dendrites contained in the entire DR volume).

3.2. Strength, load partition and deformation mechanisms

3.2.1. Nanoindentation
Nanoindentation was carried out to characterize hardness and elastic modulus of the phases individually. The results are summarized in Table 3, where H and E_I are the hardness and the indentation modulus, respectively. The hardness of η-Ti$_4$Fe$_2$O$_x$ is more than twice as high as that of β-Ti, whereas the intermetallic TiFe phase is only ~ 20% harder than β-Ti (Table 3). These results agree with previous reports (η: 907 $\pm$ 82 HV, β: 450 $\pm$ 21 HV, TiFe: 481 $\pm$ 44 HV [22]). The indentation modulus E_I is similar for TiFe and η-Ti$_4$Fe$_2$O$_x$ (~ 200 GPa) and lies close to the Young's modulus (~ 210 GPa) reported by Zhu et al. for TiFe [24].

3.2.2. In-situ compression testing
The engineering stress-strain relationship (σ_E - $\varepsilon_{E,p}$) obtained for LPBF-Ti-32.5Fe (T_{PH} = 790 °C, E_V = 178 J/mm^3) during in situ compression test at 600 °C demonstrates high strength and large deformation. The results are shown in Fig. 7, together with the evolution of lattice strains (ε_L) in the axial direction for selected lattice planes of β-Ti, TiFe and η-Ti$_4$Fe$_2$O$_x$, where only the plastic deformation is considered. σ_E denotes the engineering stress while $\varepsilon_{E,p}$ corresponds to the plastic engineering strain.

The lattice strains show strong variations between the different lattice planes: We either observed a steady increase of ε_L until the end of the experiment at $\varepsilon_{E,p}$ ~ 0.3 (e.g. {100}TiFe), the occurrence of a plateau after reaching a certain strain ({110}TiFe) or a maximum followed by a decrease of ε_L (e.g.{211}TiFe). The highest

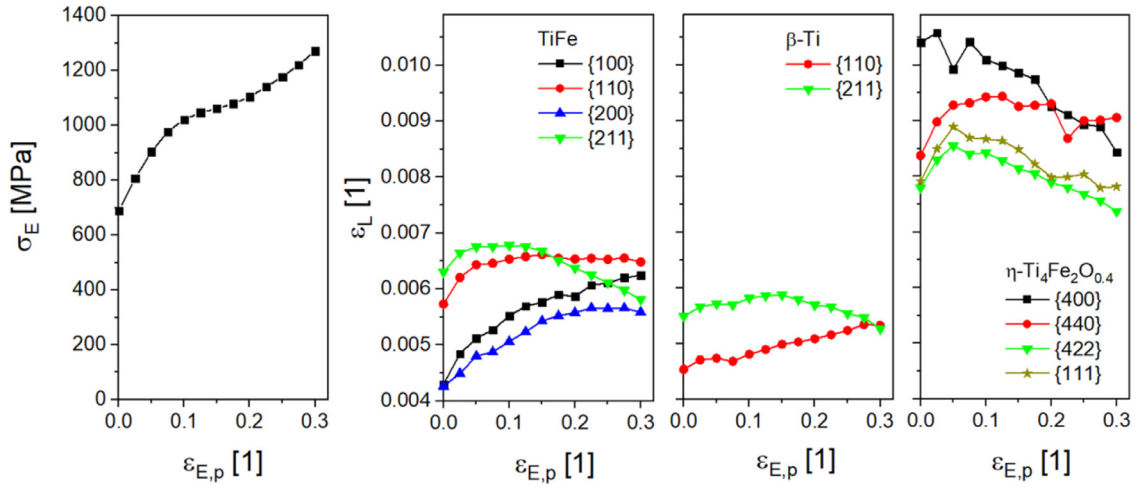**Fig. 7.** Engineering stress-strain ($\sigma_E - \varepsilon_{E,p}$) relationship and evolution of characteristic lattice strains (ε_L) of selected lattice planes of TiFe, β-Ti and η-Ti$_4$Fe$_2$O$_x$ obtained during uniaxial compression at 600 °C. Note that the ε_L axis starts at 0.004.
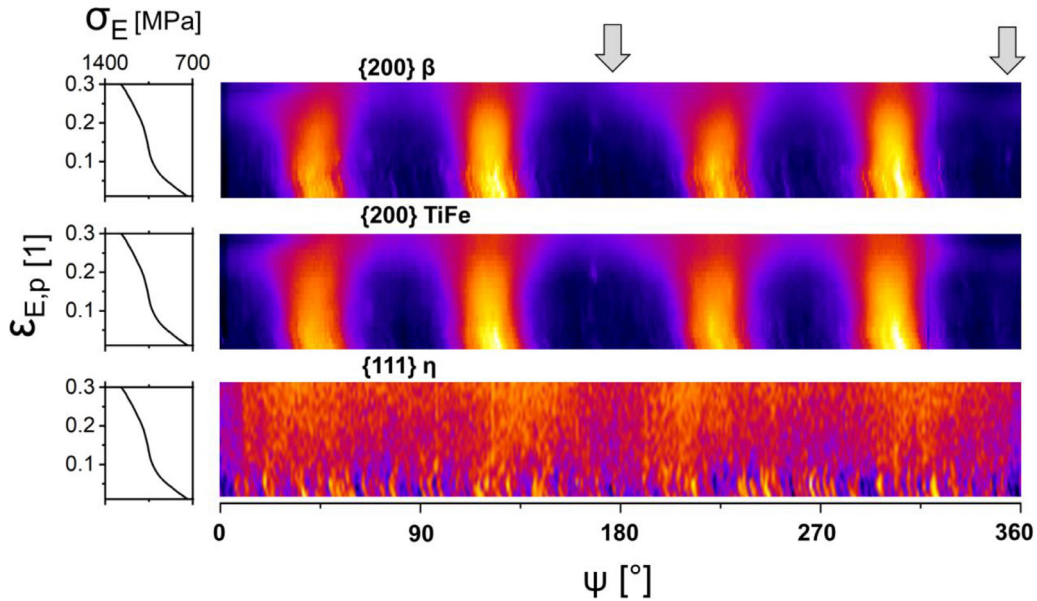

Fig. 8. Colour-coded 2D plots showing the evolution of {200}β, {200}TiFe and {111}η Bragg reflection intensities for the azimuthal range ($\psi = 0$–360°) during plastic deformation under uniaxial compressive loading at 600 °C. Load direction is indicated by grey arrows and was parallel to the building direction of the LPBF sample.

lattice strains were reached for the η phase, i.e. $\varepsilon_{L,max} \sim 0.008$ for {442}η up to ~ 0.011 for {400}η, in contrast to $\varepsilon_{L,max} \sim 0.0055$–0.007 for TiFe. All considered lattice planes of η show a clear maximum and a subsequent decrease of ε_L, though ε_L remains fairly constant after this maximum in the case of {440}η.

The evaluation of the lattice strains of the β-Ti phase is limited to {110}β and {211}β because of the superposition between {200}β and {551}η reflections. For {110}β a short plateau at $\varepsilon_L \sim 0.0047$ is followed by a steady increase to ~ 0.0053 at $\sigma_{E,p} \sim 0.3$, while {211}β shows a qualitative behaviour similar to that of {211}TiFe.

The evolution of the intensity of individual Bragg reflections along the azimuthal angle ψ provides further insights into the deformation behaviour of the phases (Fig. 8). In the as-built condition, the highest intensities for the {200}β and {200}TiFe reflections are both alternately located every $\sim 75°$ and $\sim 105°$ along the ψ axis owing to the orientation relationship between β-Ti and TiFe and a <111> fibre texture of these phases (maxima would ideally be located alternately every 70° and 110°). The first maxima are

displaced $\sim 45°$ with respect to the compression axis indicated by grey arrows (the compression axis is parallel to the build direction).

This kind of texture is not found in the as-built condition of $\alpha+\beta$ titanium alloys produced by LPBF, which usually show a preferred <100> orientation in build direction of the prior β grains [25]. Also in β titanium alloys such as Ti-Cr the <100> crystallographic texture is usually observed [26].

There was virtually no texture for η-Ti$_4$Fe$_2$O$_x$ before deformation, while more or less homogeneously distributed individual reflections can be seen along the azimuth axis.

After the onset of plastic deformation, the reflections of all three phases show a trend towards a more homogeneous distribution of intensities along the ψ axis, although the dominating <111> texture remains for β-Ti and TiFe, which is plausible as it is a typical deformation texture for compression of bcc metals [27]. The homogenization of intensities along the ψ axis is particularly clearly observed for the {111}η reflection (Fig. 8).
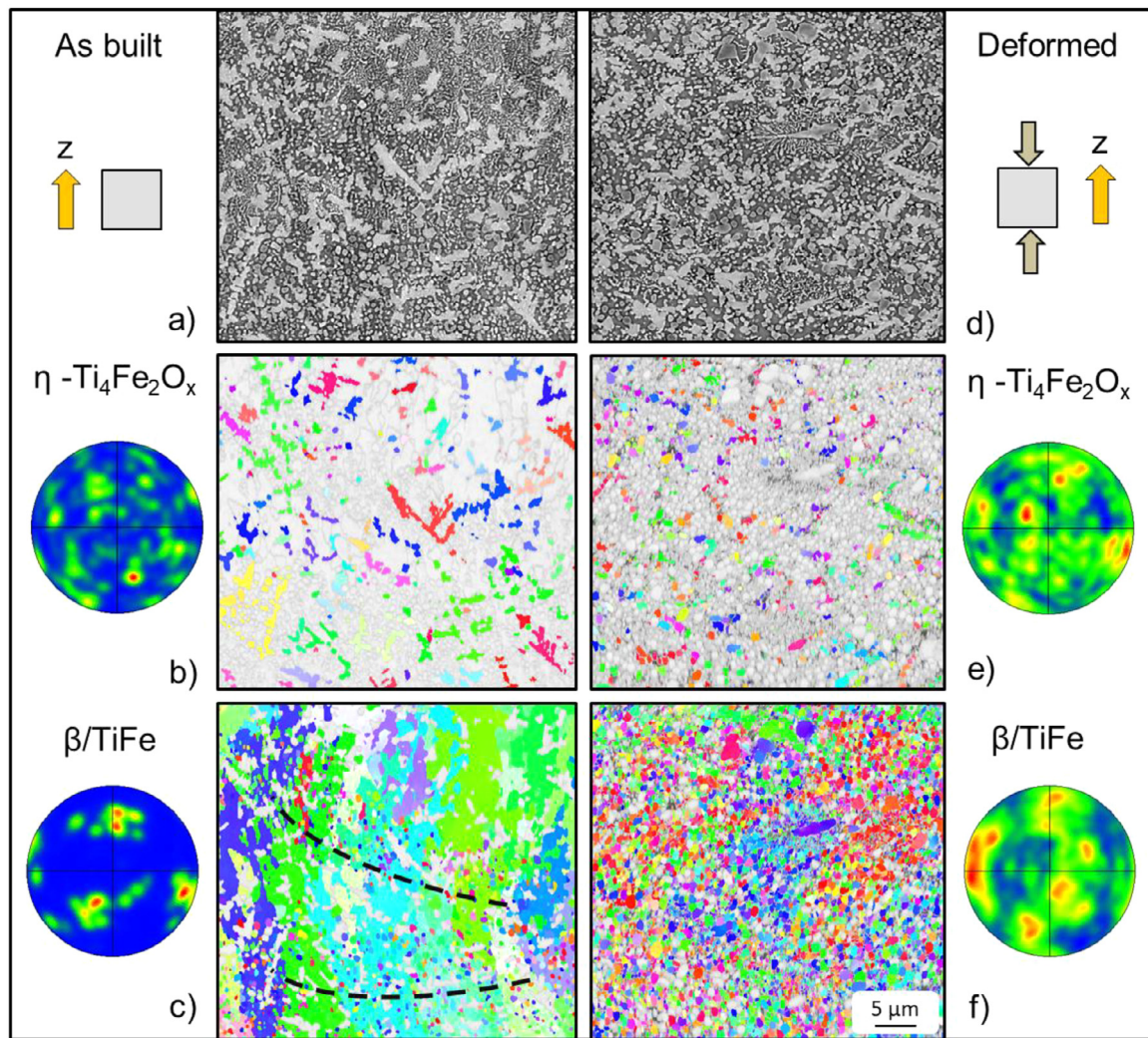
Fig. 9. Microstructure of LPBF-Ti-32.5Fe (T_{PH} = 790 °C, E_V = 178 J/mm^3). Undeformed state (a-c), and after ~ 30% compressive strain at 600 °C (d-f). SEM micrographs (a,d), IPF of η-Ti$_4$Fe$_2$O$_x$ (b,e) and IPF of β-Ti/TiFe (c,f) . Legend for IPF as in Fig. 10d. Corresponding {100} pole figures of η-Ti$_4$Fe$_2$O$_x$ (b,e) and β-Ti/TiFe (c,f) . Build direction (z) and compression direction indicated by arrows (a,d).

3.2.3. Deformed microstructure

SEM and EBSD investigations before and after compression (Fig. 9) reveal further details on the deformation mechanisms active in LPBF-Ti-32.5Fe (T_{PH} = 790 °C, E_V = 178 J/mm^3). The η-Ti$_4$Fe$_2$O$_x$ dendrites present random crystallographic orientations prior to deformation (Fig. 9a and b). The surrounding β-Ti/TiFe eutectic structures exist as colonies with β-Ti and TiFe showing the "cube-on-cube" crystallographic orientation relationship $<100>(100)_{\beta\text{-Ti}} \parallel <100>(100)_{\text{TiFe}}$ [3] and are, therefore, not discernible individually in the inverse pole figure (IPF) map (Fig. 9c). The size of the colonies is difficult to estimate but they extend roughly 20–30 µm in the build direction, and around 5 µm in the transverse direction.

While the SEM micrograph of the deformed condition (Fig. 9d) appears similar to the undeformed state, the IPF maps and EBSD texture analysis present clear differences:

1) The η-Ti$_4$Fe$_2$O$_x$ dendrites are fragmented into fairly equiaxed grains with different crystallographic distributions, even for fragments that seem to have belonged to one individual dendrite (Fig. 9e). As a result, the fragmented dendrites introduce a larger number of crystallographic orientations in comparison to the as-built condition. This agrees with the effects observed

in Fig. 8 that show that the individual reflections of this phase tend to vanish as plastic deformation advances.

2) The relatively large and irregularly shaped β-Ti/TiFe colonies present in the undeformed condition are fragmented into equiaxed regions (sub-colonies) with diameters of mostly 1–2 µm after deformation (Fig. 9f), while there is a decrease in texture with respect to the as-built condition.

The EBSD results also reveal the presence of globular TiFe particles of ~ 1 µm in diameter in the as-built condition at the bottom of the melt pools (see Fig. 9c – the bottoms of the melt pools are indicated by dashed lines). Similar equiaxed grains were reported to be formed as a result of incomplete re-melting at the interlayer boundaries between consecutive powder depositions in a eutectic Fe-Fe$_2$Ti alloy produced by directed energy deposition [28].

A detailed view of the EBSD results before (Fig. 10a–c) and after (Fig. 10e–g) deformation clearly shows fragmentation and rotation of η-Ti$_4$Fe$_2$O$_x$ dendrites (see e.g. Fig. 10f, area 1 and 5 in comparison to Fig. 10b, area 1 and 5). Also, the β-Ti/TiFe colonies, which appear as a single grain in the IPF map, fragmented into fine globular grains with various crystal orientations as can be clearly seen by comparing Fig. 10c and g. The presence of globular TiFe grains (Fig. 10c, see area 2 and 4) can only be distinguished from the η-Ti$_4$Fe$_2$O$_x$ dendrites by EBSD.
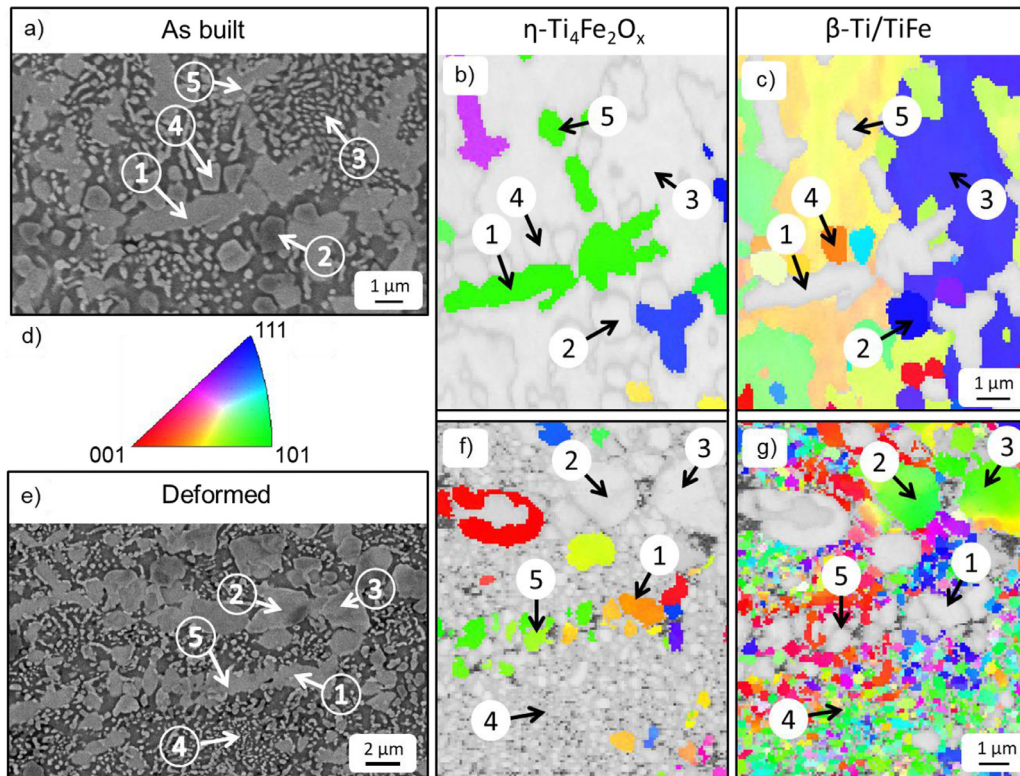
Fig. 10. Comparison of local microstructure and EBSD maps in LPBF-Ti-32.5Fe (T_{PH} = 790 °C, E_V = 178 J/mm^3) before (a–c) and after (e-g) ~ 30% compressive strain at 600 °C. SEM images (a and e), IPF of η-Ti$_4$Fe$_2$O$_x$ (b, f), and IPF of β-Ti/TiFe (c and g). Legend for IPF maps (d).

4. Discussion

4.1. Microstructure formation and assessment

Heinen [14] investigated the microstructure formation during solidification of electromagnetically levitated samples of Ti-30.5Fe-1.3O (wt.%) and Ti-30.2Fe-2O (wt.%) alloys by in situ X-ray diffraction. He observed that the first phase to form was α-Ti, which was stabilized by a large fraction of oxygen (O ~ 20 at.%), followed by the nucleation and growth of η-Ti$_4$Fe$_2$O$_x$. The remaining melt solidified eutectically forming β-Ti and TiFe. Thus, the microstructure formation path of these near eutectic alloys can be summarized as L → L + α-Ti → L + α-Ti + η-Ti$_4$Fe$_2$O → α-Ti + η-Ti$_4$Fe$_2$O + β-Ti + TiFe.

The presence of η-Ti$_4$Fe$_2$O$_x$ dendrites in our investigations for LPBF-Ti-32.Fe (wt%) processed with E_V > 160 J/mm^3 suggests the following sequence of microstructure formation: First, η-Ti$_4$Fe$_2$O$_x$ dendrites solidify in the melt, hence a random texture is obtained for this phase in the as-built condition (Fig. 8). The dendrites formation is then followed by the eutectic reaction L → β-Ti + TiFe.

The discrepancy with the sequence of formation reported by Heinen [14] can be explained by two facts: i) the oxygen content in the melt during LPBF was lower than in the case of the solidification experiments [14] because we measured ~ 0.45 wt.% of oxygen in the built sample and, more importantly, ii) the cooling rates during LPBF are orders of magnitudes higher, i.e. in the order of up to 10^7 K/s [29], and suppress the nucleation of α-Ti.

The oxygen for the stabilization of η-Ti$_4$Fe$_2$O$_x$ originated probably from traces of O$_2$ in the Ar inert gas atmosphere during the LPBF process, i.e., from a pickup of oxygen by the hot melt pool and during solid state reaction of the powder and the laser-melted upper surface layer of the samples.

The small amounts of α-Ti found primarily at the boundaries of eutectic β-Ti/TiFe colonies (Figs. 2 and 3) point to their formation by a eutectoid reaction β-Ti → α-Ti + TiFe, during cooling of the baseplate after the LPBF process.

The main constituents of the material in the as-built condition are the three phases TiFe, β-Ti and η-Ti$_4$Fe$_2$O$_x$, with structures similar to those obtained for hypo- and hypereutectic alloys produced by rapid solidification [2,9]. However, a comparison with literature indicates that the dendrites as well as the eutectic regions are finer in the LPBF material, probably due to even faster solidification rates. Zhang et al. [30] reported dendrite lengths between 50 and 100 μm, primary dendrite trunks between 10 and 25 μm and secondary branches between 2 and 4 μm. In contrast, the primary branches of η-Ti$_4$Fe$_2$O$_x$ dendrites in our LPBF material are typically a few micrometres long and ~ 1 μm thick (Figs. 3, 5c and 6). EBSD revealed that the dendritic (single) crystals with their primary and secondary branches partially cover areas exceeding 10 × 10 μm^2 (Fig. 9b), while 3D imaging shows more clearly the complex interconnected shapes of the dendrites (Figs. 3d, 4d and h).

The eutectic lamellar or fibrous colonies [31] are a consequence of multiple simultaneous growth processes. The size of the colonies is a measure of the nuclei density resulting from undercooling of the melt. Colony diameters of around 20–50 μm have been reported for the binary Ti-Fe system [32,33]. The EBSD maps (Fig. 9) show that the colonies formed during LPBF are extended in the build direction (~ 20 μm), with a transverse thickness of 5–10 μm, which is in agreement with the NF-PXCT results (Fig. 2).

A recent compilation by Chanda et al. [31] shows inter-lamellar spacings, or lamellar widths, above 1 μm for binary hypereutectic alloys [30], while spacings > 300 nm (~ 1 μm [32], 525 nm [1], 300–500 nm [33]) are generally reported for eutectic compositions.

Significant refinements have been achieved by alloying in the case of conventional rapid solidification techniques. For instance, a reduction of the inter-lamellar spacing from 800 to 300 nm [34] or from 500–700 nm to even 100–150 nm [35] was observed by Sn addition (3 at.%). While these size ranges are close to the lamellar width observed in the LPBF-Ti32.5Fe (Fig. 6), the eutectic structures obtained in the present work can reach even smaller sizes (see Fig. 3c).

Moreover, the ER region contains colonies with different sizes ranges (see e.g. R1 to R3 in Fig. 5a and b) that present mean lamellar widths between ~ 90 and ~ 160 nm. Hierarchical eutectic structures, i.e., finer eutectics coexisting besides coarser colonies were also reported by Cao et al. [8]. The hierarchical features in the microstructure of the LPBF alloy reach even smaller sizes, as revealed by the interdendritic colonies in the DR region, that fall close to resolution limit of NF-PXCT (Fig. 2b and d), i.e. an estimation of the lamellar width around 30–50 nm seems reasonable.

4.2. High temperature deformation

Various studies demonstrate outstanding mechanical properties at room temperature for ultrafine eutectic Ti-Fe-based alloys [31], while their high temperature behaviour has received, to the best knowledge of the authors, no attention.

Shear-banding is considered to be a main deformation mode in a nanostructured / ultrafine eutectic matrix [36,37]. In this case, localized shear bands can lead to deformation instabilities and premature failure, while shear-instabilities can be overcome by introducing structural and spatial heterogeneities [37].

The microstructure of LPBF-Ti-32.5Fe (T_{PH} = 790 °C, E_V = 178 J/mm^3) after deformation at 600 °C does not show any indication of localized shear banding. Similar to the effect of TiFe dendrites in the hypereutectic systems [38], the η-Ti$_4$Fe$_2$O$_x$ dendrites may act as a structural heterogeneity that allows a uniform plastic deformation. The alloy was deformed plastically up to $\varepsilon_{E,p}$ ~ 0.3 without damage formation, which can be explained mainly by the fact that, in contrast to the more brittle behaviour at RT, the deformability of TiFe (and other B2 intermetallics, as e.g. reported for NiAl: ε_p > 40% at 600 °C [39]) is strongly enhanced at high temperatures. This suggests that both β-Ti and TiFe deform plastically by dislocation slip, and that slip transfer from A2 to B2 is facilitated. The broadening of the diffraction reflections and the spreading of the dominating texture observed during compression, exemplarily shown for {200}β and {200}TiFe in Fig. 8, indicate strong dislocation activity during deformation. Moreover, the homogenization of the reflection intensity profile along ψ also indicates plastic deformation of η-Ti$_4$Fe$_2$O$_x$ (Fig. 8).

In-situ HEXRD revealed very high elastic lattice strains for η-Ti$_4$Fe$_2$O$_x$ phase in comparison to the β-Ti and TiFe phases, suggesting a higher strength of this phase during high temperature deformation (Fig. 7). This is supported by room temperature nanoindentation results, in which hardness > 12 GPa was found for η-Ti$_4$Fe$_2$O$_x$ in contrast to 7.6 GPa and 6.2 GPa for TiFe and β-Ti, respectively. TiFe and η-Ti$_4$Fe$_2$O$_x$ have similar Young's moduli of ~ 200 GPa at room temperature (Table 3), and it seems reasonable to assume that these should not differ much at 600 °C. It can be therefore inferred that η-Ti$_4$Fe$_2$O$_x$ has a higher load bearing capability than TiFe. While all phases contribute to the high temperature strength by bearing part of the load, the presence of η-Ti$_4$Fe$_2$O$_x$ provides a further increase in the high temperature strength of the alloy. In addition to the high strength and stiffness, the morphology of η-Ti$_4$Fe$_2$O$_x$ is considered to contribute to the material performance, as rigid phases with high aspect ratios can bear higher loads than spherical particles [40]. Moreover, the relatively coarse network of η-Ti$_4$Fe$_2$O$_x$ dendrites (with high aspect ratio) may act as reinforcement during creep exposure [41], as long as the dendrites are not fragmented to particle-like entities, which are considered less effective as reinforcement during creep exposure [42].

The lattice strains of η-Ti$_4$Fe$_2$O$_x$ decrease after reaching a maximum at $\varepsilon_{E,p}$ ~ 0.05 (Fig. 7), which coincides with the strain at which the individual diffraction spots along the ψ axis begin to blur (see {100}η in Fig. 8). This blurring can be connected to the fragmentation of η-Ti$_4$Fe$_2$O$_x$ dendrites into small equiaxed grains with the wider spread of crystallographic orientations shown by the EBSD results (Figs. 9e and 10f). The morphological change experienced by this phase reduces its load bearing capability and may be the reason for the plateau observed in the stress-strain curve. The continuous lattice strain increase of {100}TiFe suggests a load transfer from η-Ti$_4$Fe$_2$O$_x$ to TiFe and strain hardening at higher degrees of deformation (Fig. 7).

The eutectic colonies (~ 20 µm) are transformed into fine mainly globular regions (1–2 µm) during deformation (Fig. 9). We hypothesize that these sub-colonies are the result of a rotational deformation mechanism similar to that proposed by Zhu et al. [3] in which the refinement of the relatively large colonies allows reorientation of the sub-colonies to facilitate dislocation slip. Additionally, gliding along the new arising sub-colony boundaries may also contribute to the deformation mechanism at high temperature [1].

5. Conclusions

A dense and crack-free Ti-32.5Fe alloy has been produced by LPBF. Applying an effective baseplate temperature of ~ 600 °C the oxygen content increased to ~ 0.45 wt.%, and at high energy densities the alloy was composed mainly of the phases TiFe, β-Ti, η-Ti$_4$Fe$_2$O$_x$ and small amounts of α-Ti. The results indicate that Ti$_4$Fe$_2$O$_x$ is thermodynamically stable at 600 °C.

The primary dendritic η-Ti$_4$Fe$_2$O$_x$ structures are embedded in the matrix of ultrafine eutectic β-Ti/TiFe colonies with mean lamellar widths from ~ 160 nm down to ~ 50 nm. The hierarchical ultrafine microstructure was revealed three-dimensionally by NF-PXCT and are the finest structures reported so far for bulk eutectic binary Ti-Fe.

The alloy was plastically compressed ~ 30% at 600 °C without damage formation, demonstrating good compressive high temperature ductility of the LPBF alloy. Moreover, the compressive yield strength of the alloy reaches ~ 800 MPa at this temperature, demonstrating the potential of the alloy for applications at intermediate temperatures. Without considering any tension-compression anisotropy, the specific yield strength of ~ 140 MPa/(g/cm^3) obtained for LPBF-Ti32.5Fe at 600 °C is far above that of near-α Ti alloys such as IMI 834 (~ 110 MPa/(g/cm^3)) and close to that of IN718 [43].

The high load bearing capability of η-Ti$_4$Fe$_2$O$_x$, and its dendritic morphology with its high aspect ratio contribute substantially to the high temperature performance of the material.

The present study provides a first demonstration of the feasibility to produce eutectic and near-eutectic Ti-Fe alloys by LPBF with ultrafine microstructures and mechanical strength as well as compressive ductility attractive for structural applications. As a more general contribution, this works provides clear insights for materials design exploiting the rapid solidification capabilities of laser-based additive manufacturing.

Data availability

Experimental data from this study are available from the corresponding author upon reasonable request.

Declaration of Competing Interest

The authors declare that they have no known competing financial interests or personal relationships that could have appeared to influence the work reported in this paper.

CRediT authorship contribution statement

Joachim Gussone: Investigation, Methodology, Visualization, Writing - original draft. **Katrin Bugelnig:** Investigation, Visualization, Writing - review & editing. **Pere Barriobero-Vila:** Investigation, Writing - review & editing. **Julio Cesar da Silva:** Methodology, Investigation, Writing - review & editing. **Ulrike Hecht:** Conceptualization, Funding acquisition, Writing - review & editing. **Christian Dresbach:** Investigation, Writing - review & editing. **Federico Sket:** Investigation, Funding acquisition, Writing - review & editing. **Peter Cloetens:** Methodology, Investigation, Writing - review & editing. **Andreas Stark:** Investigation, Writing - review & editing. **Norbert Schell:** Investigation, Writing - review & editing. **Jan Haubrich:** Investigation, Funding acquisition, Writing - review & editing. **Guillermo Requena:** Conceptualization, Funding acquisition, Methodology, Investigation, Writing - original draft.

Acknowledgements

Supplementary materials

Supplementary material associated with this article can be found, in the online version, at doi:10.1016/j.apmt.2020.100767.

References

[1] J. Das, et al., Appl. Phys. Lett. 87 (2005) 161907.
[2] D.V. Louzguine-Luzgin, Mater. Trans. 59 (10) (2018) 1537.
[3] F. Zhu, et al., Appl. Phys. Lett. 98 (8) (2011) 081906.
[4] R.J. Contieri, et al., J. Cryst. Growth 333 (1) (2011) 40.
[5] J.M. Park, et al., Philos. Mag. Lett. 89 (10) (2009) 623.
[6] G.H. Cao, et al., Appl. Phys. Lett. 102 (6) (2013) 061908.
[7] G.-.H. Zhao, et al., Scr. Mater. 135 (2017) 59.
[8] G.H. Cao, et al., Cryst. Res. Technol. 49 (5) (2014) 338.
[9] L.-.C. Zhang, Adv. Mater. Res. 1 (1) (2012) 13.
[10] W. Rostocker, J. Met. (1955) 113 January.
[11] B. Rupp, P. Fischer, J. Less-Common Met. 144 (2) (1988) 275.
[12] C.S. Wang, et al., J. Mater. Sci. 43 (1) (2008) 218.
[13] O. Zemek, et al., Monatshefte für Chemie 100 (1969) 2075.
[14] O. Heinen, Nahordnung und Erstarrung unterkühlter Schmelzen von Ti-Basis Legierungen, Ruhr-Universität Bochum, 2005.
[15] A. Simchi, H. Pohl, Mater. Sci. Eng. A 359 (1) (2003) 119.
[16] F. Lasagni, et al., Acta Mater. 55 (11) (2007) 3875.
[17] J.C. da Silva, et al., Optica 4 (5) (2017) 492.
[18] M. Stockmar, et al., Sci. Rep. 3 (1) (2013) 1927.
[19] M. Guizar-Sicairos, et al., Opt. Express 19 (22) (2011) 21345.
[20] J. Schindelin, et al., Nat. Methods 9 (2012) 676.
[21] A. Cuesta, et al., IUCrJ 6 (473–491) (2019).
[22] A. Schlieter, et al., Intermetallics 19 (3) (2011) 327.
[23] Z. Asghar, et al., Acta Mater. 59 (2011) 6420.
[24] L.F. Zhu, et al., Acta Mater. 60 (4) (2012) 1594.
[25] M. Simonelli, et al., Metall. Mater. Trans. A 45 (6) (2014) 2863.
[26] T. Nagase, et al., Mater. Des. 173 (2019) 107771.
[27] L.A.I. Kestens, H. Pirgazi, Mater. Sci. Technol. 32 (13) (2016) 1303.
[28] G. Requena, et al., Addit. Manuf. 33 (2020) 101133.
[29] R.J. Hebert, J. Mater. Sci. 51 (3) (2016) 1165.
[30] L.-.C. Zhang, et al., Appl. Phys. Lett. 91 (5) (2007) 051906.
[31] B. Chanda, et al., J. Alloys Compd. 827 (2020) 154226.
[32] J. Das, et al., J. Alloys Compd. 434-435 (2007) 28.
[33] C.H. Lee, et al., Mater. Des. 60 (2014) 363.
[34] T. Maity, J. Das, J. Alloys Compd. 585 (2014) 54.
[35] J.H. Han, et al., Met. Mater. Int. 17 (6) (2011) 873.
[36] G. He, et al., Nat. Mater. 2 (1) (2003) 33.
[37] G.A. Song, et al., Intermetallics 23 (2012) 27.
[38] D.V. Louzguine, et al., J. Mater. Res. 19 (12) (2004) 3600.
[39] A.M. Russell, Adv. Eng. Mater. 5 (9) (2003) 629.
[40] T.W. Clyne, P.J. Withers, An Introduction to Metal Matrix Composites, Cambridge University Press, Cambridge, 1993.
[41] N. Chawla, K.K. Chawla, Metal Matrix Composites, Springer, Boston, 2006.
[42] H.M.A. Winand, et al., Mater. Sci. Eng. A 284 (1) (2000) 103.
[43] S. Mayer, et al., Adv. Eng. Mater. 19 (4) (2017) 1600735.